

# Unveiling the Mechanical and Electrochemical Evolution of Nanosilicon Composite Anodes in Sulfide-Based All-Solid-State Batteries

Daxian Cao, Tongtai Ji, Avtar Singh, Seongmin Bak, Yonghua Du, Xianghui Xiao, Hongyi Xu,\* Juner Zhu,\* and Hongli Zhu\*

The utilization of silicon anodes in all-solid-state lithium batteries provides good prospects for facilitating high energy density. However, the compatibility of sulfide solid-state electrolytes (SEs) with Si and carbon is often questioned due to potential decomposition. Herein, operando X-ray absorption near-edge structure (XANES) spectroscopy, ex situ scanning electron microscopy (SEM), and ex situ X-ray nanotomography (XnT) are utilized to investigate the chemistry and structure evolution of nano-Si composite anodes. Results from XANES demonstrate a partial decomposition of SEs during the first lithiation stage, which is intensified by the presence of carbon. Nevertheless, the performances of first three cycles in Si–SE–C are stable, which proves that the generated media is ionically conductive. XnT and SEM results show that the addition of SEs and carbon improves the structural stability of the anode, with fewer pores and voids. A chemo-elasto-plastic model reveals that SEs and carbon buffer the volume expansion of Si, thus enhancing mechanical stability. The balance between the pros and cons of SEs and carbon in enhancing reaction kinetics and structural stability enables the Si composite anode to demonstrate the highest Si utilization with higher specific capacities and a better rate than pure Si and Si composite anodes with only SEs.

## 1. Introduction

Growing concern about CO<sub>2</sub> emissions triggered the development of electric vehicles (EVs) to replace the internal combustion engine.<sup>[1]</sup> Given current lithium-ion batteries (LiBs) using liquid electrolytes cannot meet the greatly increased demand for energy density and safety, it is of significance to develop new generation batteries.<sup>[2]</sup> All-solid-state lithium batteries (ASLBs), based on nonflammable solid-state electrolytes (SEs), are expected to boost the energy density through a unique bipolar stacking and relief the safety concern.<sup>[3]</sup> However, batteries based on conventional LiCoO<sub>2</sub> cathode and graphite anode have reached the theoretical limitation to energy density.<sup>[4]</sup> It is urgent to employ high-capacity electrode materials in developing high-energy ASLBs.<sup>[4]</sup>

Among various anode candidates, silicon (Si), possessing an ultrahigh specific capacity of 3590 mAh g<sup>-1</sup> at room temperature (around ten times higher than graphite anode), is regarded as one of


the most promising anode materials for LiBs.<sup>[5]</sup> The moderate working potential of 0.4 V (vs Li<sup>+</sup>/Li) enables the Si-based LiBs with low dendrite growth risk and high energy density.<sup>[5]</sup> Since 2007, different types of Si, like the thin film Si<sup>[6]</sup> (<1 μm in thickness), nano-Si<sup>[7]</sup> (50–100 nm in diameter), and micro-Si<sup>[8]</sup> (1–5 μm in particle size), have been applied in ASLBs using polymers, oxides, and sulfides as SEs.<sup>[9]</sup> Specifically, the ASLBs using sulfide SEs deliver prominent performances, because sulfide SEs<sup>[10]</sup> own a remarkable ionic conductivity (>1 mS cm<sup>-1</sup>) at room temperature and intimate contact with electrode materials. However, a recent work<sup>[8b]</sup> reported that the sulfide SE shows instability in the Si anode during electrochemical reactions, and the addition of carbon accelerates the decomposition of the sulfide SE, resulting in the increased impedance for ion/electron conduction and corresponding battery performance decay. To circumvent this side reaction, Tan et al.<sup>[8b]</sup> use pure micro-Si (1–5 μm) as the anode without adding SE and carbon in the anode. The full cell delivers outstanding cycling stability for 500 cycles with a capacity retention of 80% at the current density of 5 mA cm<sup>-2</sup>.<sup>[8b]</sup> However, due to ≈300% volume

D. Cao, T. Ji, J. Zhu, H. Zhu  
Department of Mechanical and Industrial Engineering  
Northeastern University  
Boston, MA 02115, USA  
E-mail: j.zhu@northeastern.edu; h.zhu@neu.edu

A. Singh  
Center for Energy Conversion and Storage Systems  
National Renewable Energy Laboratory  
Golden, CO 80401, USA

S. Bak, Y. Du, X. Xiao  
National Synchrotron Light Source II  
Brookhaven National Laboratory  
Upton, NY 11973, USA

H. Xu  
Department of Mechanical Engineering  
University of Connecticut  
Storrs, CT 06269, USA  
E-mail: hongyi.3.xu@uconn.edu

 The ORCID identification number(s) for the author(s) of this article can be found under <https://doi.org/10.1002/aenm.202203969>.

DOI: 10.1002/aenm.202203969

change occurring in the Si anode, micrometer-sized voids are observed in pure Si anode after delithiation, which brings a great risk of electrode delamination. In comparison, nano-Si (<100 nm) exhibits higher structural stability and fewer voids formation because the smaller size can potentially relieve the stresses. In our previous work, we reported that the ASLBs using a nano-Si-based composite anode deliver a long cycling life of 1000 cycles. No huge voids are observed, except for some vertically grown cracks.<sup>[11]</sup> Most reported nano-Si-based anodes<sup>[3a,7,8a,11,12]</sup> are composites with SE and carbon additives because nano-Si has low electronic conductivity and low ion diffusivity. Questions come on the nano-Si-based composite anode: what are the effects of adding SE and carbon to 1) the battery performance, 2) the (electro-)chemical stability of the sulfide SE, and 3) the electrode structure evolution?

To answer these questions, herein, we systematically analyzed the chemistry and structure evolution of nano-Si-based composite anodes via operando synchrotron X-ray absorption near-edge structure (XANES) spectroscopy and ex situ scanning electron microscopy (SEM) combined with ex situ X-ray nanotomography (XnT). We investigated three kinds of nano-Si-based anodes: pure nano-Si, nano-Si compositing with SE (Si-SE), and nano-Si compositing with SE and carbon (Si-SE-C). XANES is highly sensitive to the chemical state of the sulfur (S) element in the sulfide SE, which can be used for real-time monitoring of the stability of the SE during the test. The morphology evolutions of the nano-Si-based anodes are detected with the SEM. The XnT provides more detailed morphology information and pore distributions in a 3D view. A chemo-elasto-plastic

modeling has been constructed in order to gain deeper insights for the mechanical behavior of the three electrodes. In the end, the battery performances of the three anodes are compared to provide more evidence for the pros and cons of compositing Si with SE and carbon.

## 2. Results and Discussion

Volume expansion and low conductivity are two major challenges with Si-based anode. Si is known as a semiconductor with electronic conductivity of  $10^{-5} \text{ S cm}^{-1}$ .<sup>[13]</sup> Meanwhile, the ion diffusivity in the Si is in the range of  $10^{-16}$  to  $10^{-8} \text{ cm}^2 \text{ s}^{-1}$ .<sup>[14]</sup> Thus, a general consideration is adding carbon and SEs to promote both electron and ion conductions. However, as aforementioned, sulfide SEs are nonstable at the anode and the carbon can accelerate their decomposition.<sup>[8b]</sup> Therefore, it is significant to have a fundamental evaluation of the pros and cons of compositing Si with carbon and SEs. This work specifically investigated the effects of adding sulfide SE and carbon additives into the nano-Si-based anode, in terms of the reaction kinetics and stability in ASLBs, to further pave the way for the practice application of the ASLBs based on nano-Si anode.

As illustrated in **Figure 1**, three kinds of anodes based on nano-Si are designed in this work, and the effects of adding SE and carbon on the chemical and structural evolutions are investigated. In Si-SE-C (Figure 1a), three components are chemically stable before the battery test. The carbon and SE build the

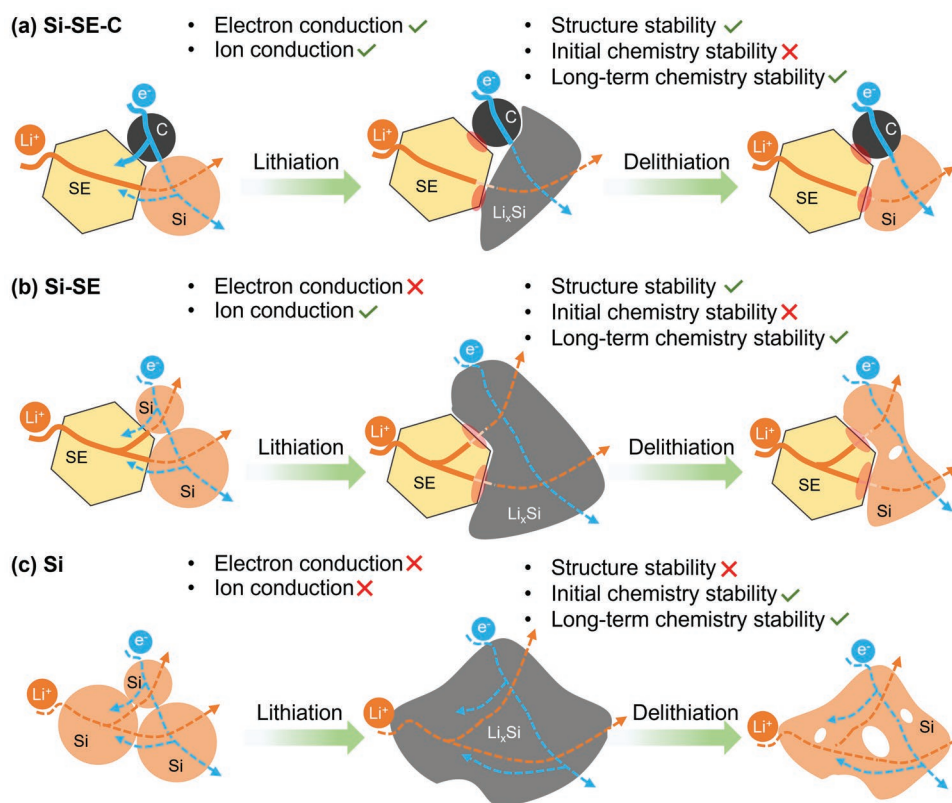


**Figure 1.** Schematic illustrating the chemistry and structure evolution of a) Si-SE-C, b) Si-SE, and c) Si anodes in ASLBs.

electron and ion conduction pathways in the composite anode separately, which enable good electron and ion accessibility to the Si anode. The SE investigated here is  $\text{Li}_{5.4}\text{PS}_{4.4}\text{Cl}_{1.6}$ , a typical argyrodite sulfide electrolyte (Figure S1, Supporting Information) owning a high ionic conductivity of  $\approx 8 \text{ mS cm}^{-1}$ . The nano-Si exhibits a high crystallinity (Figure S2, Supporting Information). During the lithiation process, the Si transforms into  $\text{Li}_x\text{Si}$  and undergoes an amorphization. At the same time, the SE, besides the Si and carbon, are electrochemically reduced, accompanied by the formation of the newborn interface layer. Theoretically, the final decomposition products are  $\text{Li}_2\text{S}$ ,  $\text{Li}_3\text{P}$ , and  $\text{LiCl}$ ,<sup>[15]</sup> which form a passivation layer at the interface. This layer causes an impedance for ion and electron conduction; despite this, it suppresses the following degradation of the SE. After delithiation, the crystalline Si becomes amorphous. The existence of SE and carbon enables an integrated electrode with less void formation. In comparison, the Si-SE experiences different processes, as illustrated in Figure 1b. The only electron conduction in the Si-SE anode is along the Si itself. Considering the surface of Si is generally covered by a thin layer of  $\text{SiO}_2$  with low electronic conductivity of  $10^{-12} \text{ S cm}^{-1}$ ,

the electron conduction in the Si-SE is relatively sluggish. Therefore, the electrochemical degradation of the SE is relieved. Similarly, Si undergoes amorphization after the delithiation. Due to the huge volume change, there are voids generated in the Si-SE anode. In contrast to the chemistry change in the composite anodes, the Si anode has good chemical stability during the lithiation and delithiation, as illustrated in Figure 1c. As the only phase, the electron conduction and ion diffusion all depend on the Si, which are lower than the conduction and diffusion along carbon and SE. In consequence, the reaction kinetic is limited. Meanwhile, the total anode experiences a huge volume change since no buffer components. After the full delithiation, there are many voids formed in the Si anode. The sluggish reaction kinetic and unstable structure challenges the nano-Si utilization and cycling stability.

Operando XANES was employed to evaluate the (electro-) chemical stability of the SE in the two Si composite anodes. Figure 2a illustrates the ASLBs under the XANES test in the fluorescence mode. We designed a special cell in which the cross-section is exposed to X-ray radiation. Constructed from a polyether ether ketone (PEEK) material, the cell consisted of a Si

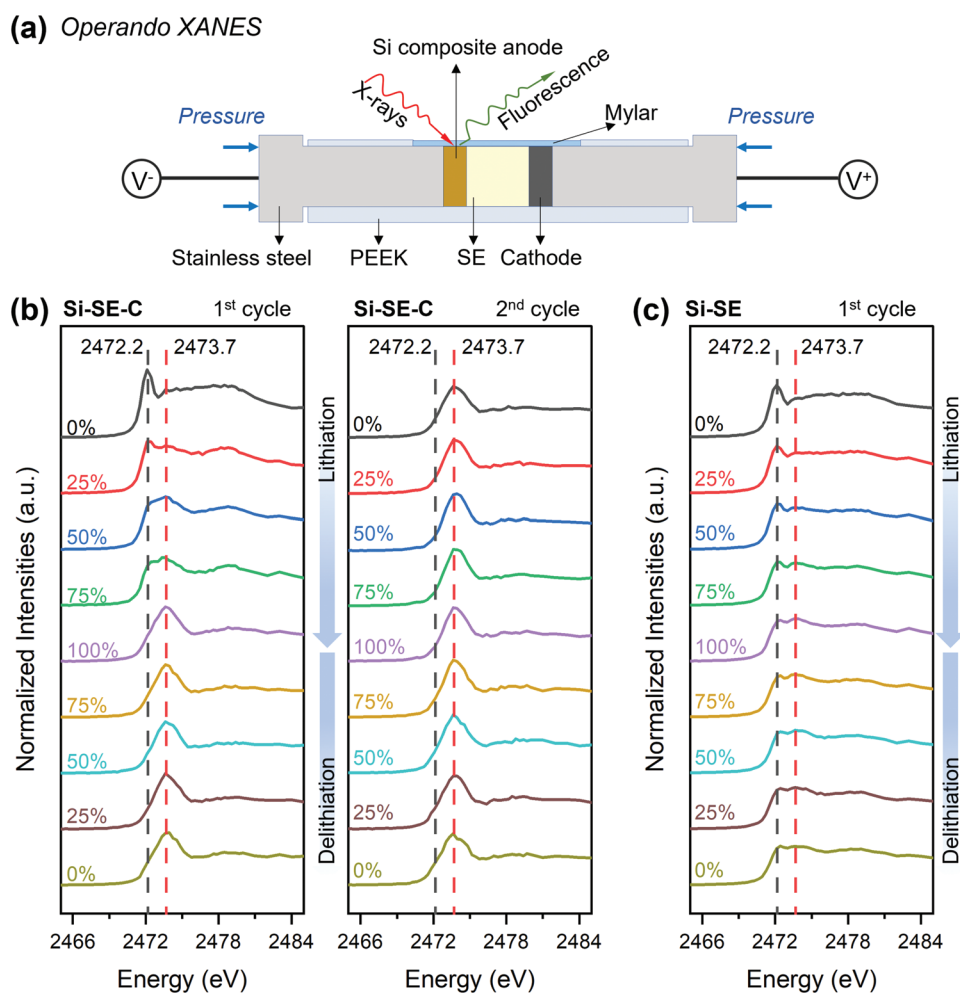


**Figure 2.** Operando investigating the chemical stability of SE in Si composite anodes. a) Schematic of the operando XANES. The sulfur K-edge XANES spectra of b) Si-SE-C composite anode at different SoC and DoD in the first two cycles, and c) Si-SE composite anode at different lithiation/delithiation states in the first cycle.

composite, SE, and a  $\text{LiNi}_{0.8}\text{Mn}_{0.1}\text{Co}_{0.1}\text{O}_2$  (NMC)-based cathode sandwiched between two stainless steel rods. The cross-section was sealed with a Mylar film, and an external framework was used to apply the required pressure. The tender X-ray excited the inner shell electron to empty or partially filled electronic states, and the detected fluorescence signals revealed the chemical state of the element. Here we evaluated the stability of the SE in Si–SE–C and Si–SE composites by observing the sulfur K-edge spectra evolution at different states of charge (SoC) and depth of discharge (DoD) during the galvanostatic charge–discharge processes (Figure S3, Supporting Information). Table S1 of the Supporting Information lists the calculated stoichiometry of  $\text{Li}_x\text{Si}$  in the two composite anodes according to the capacity.

Figure 2b displays the sulfur K-edge XANES spectra of the Si–SE–C composite at different SoC and DoD during the first two cycles. An X-ray fluorescence (XRF) mapping was conducted first to confirm the region of interest containing Si (Figure S4, Supporting Information). Before the battery test, the spectrum of Si–SE–C showed features at 2472.2, 2473.7, and 2477.7 eV, which were all assigned to the SE,  $\text{Li}_{5.4}\text{PS}_{4.4}\text{Cl}_{1.6}$ . As the gradual lithiation of Si, the peak intensity changed correspondingly: the peak at 2472.2 gradually faded, while the peak at 2473.7 gradually rose and dominated at the highest lithiation state. The spectrum change suggests that the structure of the SE changed during the Si lithiation process. Theoretically, the final products of the degraded SE are  $\text{Li}_2\text{S}$ ,  $\text{Li}_3\text{P}$ , and  $\text{LiCl}$ .<sup>[16]</sup> In our results, it does not fit the  $\text{Li}_2\text{S}$  well, especially in the main peak intensity (Figure S5, Supporting Information), which is attributed to the self-absorption issue in the XANES test and the existence of unreacted SE. In our previous work,<sup>[11]</sup> the product was identified as  $\text{Li}_2\text{S}$  through X-ray photoelectron spectroscopy. During the delithiation of Si, the XANES spectra show no obvious change even at the highest delithiation state, evidencing the irreversible decomposition of the SE is passivated by the decomposition products, i.e.,  $\text{Li}_2\text{S}$ ,  $\text{Li}_3\text{P}$ , and  $\text{LiCl}$ . In the second cycle, the spectra show no obvious change during total lithiation and delithiation processes, which suggests that the SE decomposition mainly occurs in the first cycle and the mixture of SE and  $\text{Li}_2\text{S}$  maintains long-term chemistry stability. After the battery test, we measured the sulfur K-edge XANES spectra at other positions and found many unreacted SE (Figure S6, Supporting Information), which demonstrates that only the SE attached to the Si and carbon has degradation.

The stability of the SE in the Si–SE composite anode was also investigated (Figure 2c). An XRF mapping was also conducted to identify the region of interest including Si (Figure S7, Supporting Information). Before the battery test, the spectrum features agree with the pure SE, further evidencing the stability between the Si and SE. Then during the lithiation process, the peaks evolution is similar to that in the Si–SE–C composite, except the peak at 2472.2 eV does not disappear even at the full lithiation state. This suggests that the degradation of the SE in Si–SE is not as severe as in the Si–SE–C, contributing to the far lower electron conduction in Si–SE than in Si–SE–C. During the delithiation process, all peaks maintain no change, proving the decomposition of the SE is irreversible and the decomposed products are relatively stable.

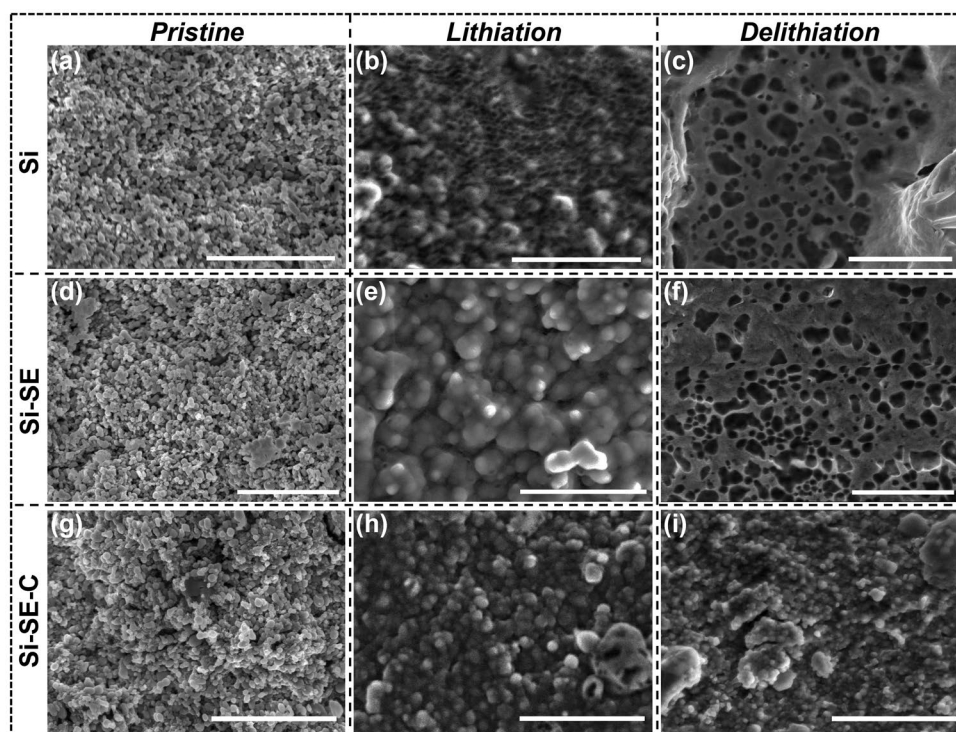
A comparison of the ex situ P and Cl K-edge XANES spectra at different lithiation states was conducted, as illustrated in

Figure S8 of the Supporting Information. The peak locations of Si–SE–C and Si–SE were similar, with only slight differences in intensity, demonstrating that the decomposition of SE in the composite sample had not been severe.

The cyclic voltammetry (CV) was conducted on the half cells of Si, Si–SE, and Si–SE–C using indium (In)–Li as a counter electrode to further evaluate the electrochemical stability of SE (Figure S9, Supporting Information). The dominant reduction peaks in all three electrodes were found to be the lithiation of Si starting from  $\approx 0.25$  V. Additionally, there are extra tiny reduction peaks in both Si–SE and Si–SE–C (Figure S9b, Supporting Information), which can be attributed to the decomposition of SE. The more distinctive peaks in Si–SE–C indicate that the decomposition of SE in Si–SE–C is more than in Si–SE, demonstrating that the addition of carbon accelerates the decomposition of SE. However, the negligible peak intensity (Figure S9a, Supporting Information) demonstrates that the decomposition of SE is not severe in both Si–SE and Si–SE–C. Furthermore, no extra oxidation peaks were observed during the delithiation process of Si, which is in agreement with the XANES result that the SE is stable during the oxidation process.

Given Si undergoes huge volume change during lithiation and delithiation, the battery performance also highly depends on the electrode structure stability, which was investigated through ex situ SEM. All the lithiation and delithiation were processed in half cells, and then Si electrodes at the lowest (lithiation) and highest (delithiation) cutoff voltages were extracted for SEM observation. Both top view (Figures S10–S12, Supporting Information) and cross-section (Figure 3; Figure S13, Supporting Information) of the electrode layer were observed. Before the battery test, Si (Figure 3a), Si–SE (Figure 3d), and Si–SE–C (Figure 3g) electrodes all show a dense structure made of nanoparticles. Although a high pressure of 300 MPa was applied in the cell stacking process, the Si particle maintains the sphere morphology without pulverization (Figure S14, Supporting Information). The SE shows a mud-like morphology (Figure S15, Supporting Information). The soft property of SE enables an intimate contact with Si nanoparticles. In comparison to the Si, the surfaces of Si–SE and Si–SE–C electrodes are denser because of the dispersing of SE and SE–C into the Si particles. Noted some regions in Si–SE–C show different contrast (Figure S16, Supporting Information), which is caused by the aggregation of SE and C.

During lithiation, Li gradually alloys with Si forming  $\text{Li}_x\text{Si}$ , accompanied by a volume expansion. The nanoparticles in Si (Figure 3b), Si–SE (Figure 3e), and Si–SE–C (Figure 3h) electrodes become mud-like amorphous morphology. This agrees with the reported process that Si becomes amorphous during lithiation.<sup>[5]</sup> Noted a high external pressure of 150 MPa was applied during the battery test. Because the amorphous  $\text{Li}_x\text{Si}$  owns lower mechanical strength than pure Si, the total electrodes are densified by the deformation of  $\text{Li}_x\text{Si}$  under the external pressure and internal stresses from the volume expansion. In the cross-section view (Figure S13b,e,h, Supporting Information), all electrodes maintain integrity without cracks and voids. From the top view, the Si anode (Figure S10h, Supporting Information) is made of large aggregations with small pores or gaps. The aggregations should be the  $\text{Li}_x\text{Si}$  (Figure S10k, Supporting Information). In comparison, there



**Figure 3.** Structure evolution investigation through ex situ SEM. Cross-section SEM images of Si anode in a) pristine, b) lithiation, and c) delithiation stages. Cross-section SEM images of Si-SE composite anode in d) pristine, e) lithiation, and f) delithiation stages. Cross-section SEM images of Si-SE-C composite anode in g) pristine, h) lithiation, and i) delithiation stages. The scale bar is 2.0  $\mu\text{m}$ .

are fewer pores or gaps between aggregations of multiple phases in both Si-SE (Figure S11h, Supporting Information) and Si-SE-C (Figure S12h, Supporting Information). Since Si-SE and Si-SE-C are composite anodes, the phases in Si-SE after lithiation should be SE and  $\text{Li}_x\text{Si}$  (Figure S11k, Supporting Information), and the phases in Si-SE-C after lithiation are SE, C, and  $\text{Li}_x\text{Si}$  (Figure S12k, Supporting Information). Moreover, the  $\text{Li}_x\text{Si}$  with varied lithiation status ( $x$  in  $\text{Li}_x\text{Si}$ ) can behave in different phases in different contrasts in SEM images. Since SE and carbon show no volume change, this confinement in the composite anode can relieve the aggregation of  $\text{Li}_x\text{Si}$  during lithiation.

After delithiation, the dealloying from  $\text{Li}_x\text{Si}$  to Si causes huge volume shrinkage, which challenges the structure stability of the Si electrodes. Notably, vertically grown reticulate cracks are observed in all three electrodes in the top view (Figures S10c, S11c, and S12c, Supporting Information) and cross-section view (Figure S13c,f,i, Supporting Information). The vertical cracks are highly related to the volume shrinkage when applied axial pressure. These cracks challenge the integrity of the electrodes affecting the cycling stability. Besides the appearance of cracks, the microstructures of all three electrodes show great changes. In the Si anode (Figure 3c), there are plenty of newly generated pores with much larger size compared with the pores in the pristine state (Figure 3a). The newly generated pores also originate from the volume shrinkage during delithiation. These pores can block the ion/electron conduction causing sluggish kinetics and capacity loss. In Si-SE, there is a similar porous structure in the cross-section (Figure 3f). In the top view

(Figure S11i, Supporting Information), there are two different morphologies: one shows a similar porous structure with the Si anode, and the other one has fewer pores. The confinement from the SE contributes to less pore generation. By contrast, Si-SE-C (Figure 3i) behaves in most stable structure. The Si-SE-C shows more homogeneous and denser morphology after delithiation than Si and Si-SE. It is because the SE and C particles dispersed in the aggregations of  $\text{Li}_x\text{Si}$  promote a uniform delithiation process and avoid the growth of large pores. For a summary, the confinement from the SE and carbon relieves the aggregation of Si during lithiation and then mitigates the pores generation during delithiation. Therefore, compositing Si with SE and carbon benefits the electrode structure stability with less pore generation and maintains good connections for charge transfer.

To further understand the effect of adding SE and carbon on structure, we utilized ex situ XnT to track the structure evolution of all three Si anodes. In comparison to the SEM, XnT can reconstruct the 3D structure of the sample and identify phases in spatial resolution ideally up to 40 nm. The actual spatial resolution depends on the contrasts between different material phases that are related to the electron densities of the materials. In this experiment, we slightly defocused the X-ray microscope to introduce the propagation phase contrast. The single-distance Paganin phase retrieval algorithm was then used to reconstruct the morphological structure of the samples with enhanced contrast between different material phases.<sup>[17]</sup> This XnT experiment was conducted in the full-field X-ray Imaging beamline (FXI/18-ID) of National Synchrotron Light

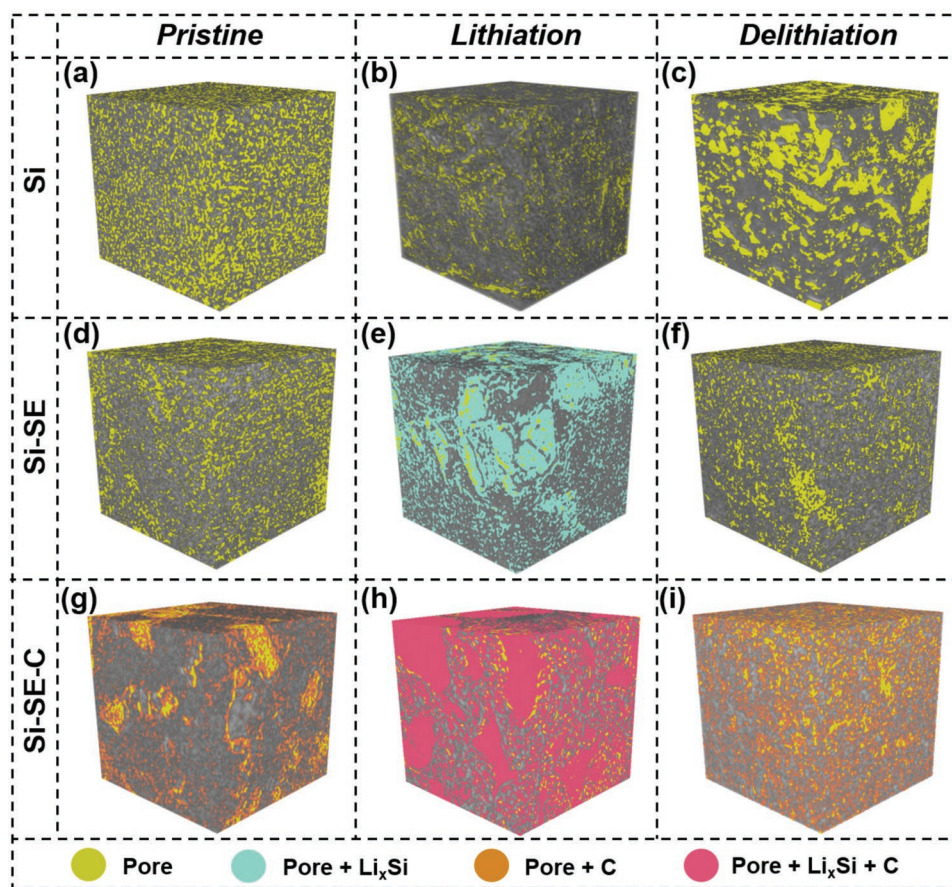


**Figure 4.** Structure evolution investigation through ex situ XnT. Reconstructed 3D structure of Si anode in a) pristine, b) lithiation, and c) delithiation stages. Reconstructed 3D structure of Si-SE composite anode in d) pristine, e) lithiation, and f) delithiation stages. Reconstructed 3D structure of Si-SE-C composite anode in g) pristine, h) lithiation, and i) delithiation stages. The cube size is  $10^*10^*10 \mu\text{m}^3$ , and the scale bar is  $5 \mu\text{m}$ .

Source II at Brookhaven National Lab.<sup>[18]</sup> To track the structure evolution, a 3D-cube in the size of  $10^*10^*10 \mu\text{m}^3$  was applied to each reconstructed sample (Figure 4). The original images filled with grayscale are listed in Figure S17 of the Supporting Information. According to the contrast differences corresponding to the X-ray attenuation, different phases in the cube are marked as different colors.

In the pristine Si anode (Figure 4a), there are only Si nanoparticles and pores in the cube. The regions with lower X-ray attenuation represent the pores in the samples and are labeled with yellow color. Similar to the SEM, the pristine Si anode shows a highly porous structure with a calculated porosity of 26.17%. These pores are the voids among Si nanoparticles. Then the structure changed a lot after lithiation (Figure 4b). The total electrode becomes denser with fewer pores observed. The Si nanoparticles are replaced with an amorphous matrix, i.e.,  $\text{Li}_x\text{Si}$ , with a larger size. The calculated porosity greatly reduces to 6.24%, which results from the volume expansion and densification of the  $\text{Li}_x\text{Si}$  under high stacking pressure during lithiation. In comparison, the porosity increases to 15.99% again after the full delithiation, deriving from the removal of Li from  $\text{Li}_x\text{Si}$  (Figure 4c). The porosity is a little lower than that in pristine Si anode because there is more Si compressed in the cube due to the deformation. However, unlike the homogeneously

distributed pores in size of several nanometers, there are some pores as large as micrometers randomly distributed in the delithiated Si anode. These pores are the result of the huge volume expansion/shrinkage of Si during alloy/dealloy processes suggesting the Si anode owns an unstable structure.

In the pristine Si-SE sample (Figure 4d), there are Si, SE, and pores in the cube. Since the electron density of Si is close to the P, S, and Cl in the SE, the contrast between Si and SE is very low. Thus, Si and SE are considered to an integrity at the pristine state. Meanwhile, the pores are still easily distinguished, which are marked with yellow color. The calculated porosity is 17.38%, lower than the pristine Si anode, suggesting that the addition of SE filled some pores among Si nanoparticles. After lithiation, the composition in the Si-SE is more complex (Figure 4e). As shown in Figure S17e of the Supporting Information, there are some regions with darker gray color than the main matrix but not as dark as the pore regions. Considering the lithiation of Si reduces the average electron density in the same subvolume, these regions are mainly assigned to the  $\text{Li}_x\text{Si}$  with a higher lithiation degree. Meanwhile, due to the low attenuation in  $\text{Li}_x\text{Si}$ , the pores in the  $\text{Li}_x\text{Si}$  are not detectable. Therefore, the pores in the  $\text{Li}_x\text{Si}$  are combined into  $\text{Li}_x\text{Si}$ , which both are marked with the cyan color. The fraction of the highly lithiated  $\text{Li}_x\text{Si}$  is less than the  $\text{Li}_x\text{Si}$  with less lithiation

(the main matrix), which demonstrates the lithiation of Si is not homogeneous in Si–SE. By contrast, the matrix in the electrode after delithiation is more homogeneous and no phase with high contrast were observed (Figure 4f). Meanwhile, there are more pores observed and some of them show aggregation in comparison to the pristine state. Nevertheless, no microscale pores are observed demonstrating considerable structure stability.

The Si–SE–C shows a different structure due to the complex composition (Figure 4g). Carbon is nearly X-ray transparent which shows a much deep gray color in the XnT. Meanwhile, since the less contrast, the pores in the carbon black are not detectable. Thus, the pores inside the carbon are combined into the carbon fraction which is marked with orange color. Similarly, Si and SE are considered to be integrity. There are carbon aggregations in the Si–SE–C electrode and most pores are also gathered at those regions. However, after lithiation, there are more regions with darker gray colors, and they take a large fraction of the electrode (Figure S17, Supporting Information). Except for the carbon aggregations, the increased region with low attenuation can be attributed to the highly lithiated  $\text{Li}_x\text{Si}$  within pores. Therefore, the carbon and highly lithiated  $\text{Li}_x\text{Si}$  within pores are combined and marked with red color in Figure 4h. The highly lithiated  $\text{Li}_x\text{Si}$  takes a large fraction of the  $\text{Li}_x\text{Si}$  and the distribution is more uniform, proving the lithiation of the Si–SE–C anode is deeper in comparison to the Si–SE anode. After delithiation, the total electrode becomes very homogenous (Figure 4i). The pore size is much smaller than that in delithiated Si anode. Meanwhile, there are less pore aggregations in comparison to the Si–SE anode. Therefore, the addition of SE–C can benefit the structural stability of the Si anode.

The electrochemical performances of the Si–SE–C, Si–SE, and Si are investigated in half cells. The mass loading of Si is  $1.42 \text{ mg cm}^{-2}$  in all electrodes. Figure 5a displays the galvanostatic charge and discharge profiles of all three electrodes in the initial cycle at the current density of  $0.1 \text{ mA cm}^{-2}$ . The Si–SE–C delivers the highest discharge/charge specific capacities of  $3288/2917 \text{ mAh g}^{-1}$  with an initial coulombic efficiency (ICE) of 88.7%. In comparison, the Si–SE contributes to relatively lower discharge/charge specific capacities of  $2653/2291 \text{ mAh g}^{-1}$  with similar ICE of 86.4%. Si anode shows the lowest discharge/charge specific capacities of  $2353/1935 \text{ mAh g}^{-1}$  with ICE of 82.2%. The highest capacities and ICE in the Si–SE–C anode demonstrates that compositing Si with SE and carbon benefits the best Si utilization. Figure 5b magnifies the charge/discharge profiles in the initial lithiation process. There is an obvious lithiation overpotential in pure Si electrode, while Si–SE–C and Si–SE directly behave flat lithiation plateaus. This overpotential is mainly caused by the sluggish ion diffusion and electron transfer in Si. Meanwhile, there are voltage slopes before the lithiation plateaus in Si–SE–C and Si–SE. One viewpoint is this slope is caused by the decomposition of the SE at higher potentials. Another reason is the enhanced reaction kinetics in composite anodes.

Electrochemical impedance spectroscopy (EIS) was utilized to evaluate the stability of the three electrodes at different lithiation states. Before the battery test, the Nyquist plots in all three cells show incomplete semicircles followed by the Warburg tails (Figure S18, Supporting Information). The interception represents the total resistance. Si–SE–C owns the lowest impedance, Si is higher, and Si–SE shows the highest impedance.

The Si–SE–C has the smallest total resistance due to the combination of carbon and SE, whereas Si–SE has a greater resistance than Si since SE has a much lower electrical conductivity than Si. Figure 5c illustrates the Nyquist plots of three cells at a completely lithiated state, along with the corresponding  $LR_1(Q_2R_2)(Q_3R_3)Q_4$  fitted profiles, as indicated in the inset. All three cells show a depressed semicircle at high and mid frequencies and a Warburg tail at low frequencies. The semicircle at mid frequency is attributed to the combined interface resistances at the Si/SE and In–Li/SE, represented as  $R_3$ . Since grain boundaries are inevitable in cold-pressed electrodes, the depressed semicircle at high frequency is considered as grain boundary resistance,  $R_2$ .  $L$  represents the inductance in the test.  $R_1$  means the total resistance in the cell. Constant phase elements (CPEs,  $Q$ ) are used for fitting. Figure 5d compares the fitted resistances of three electrodes after lithiation. Si shows the lowest interface resistance ( $7.1 \Omega$ ), Si–SE–C is higher ( $16.0 \Omega$ ), and Si–SE shows the highest value ( $31.2 \Omega$ ). Overall, the resistances in all three cells are low, demonstrating that the decomposition of SE has ignorable effects on the interface resistance. Figure 5e shows Nyquist plots of the cells after delithiation. There are no obvious semicircles but replaced with a long tail in comparison to the lithiation states. The same equivalent circuit was used to fit the plots, and the results are shown in Figure 5f. Despite the minor evolution in  $R_1$  and  $R_2$ , the interface resistance in Si and Si–SE rose to  $485.6$  and  $496.1 \Omega$ , respectively. By contrast, the  $R_3$  in Si–SE–C maintains a low value ( $11.9 \Omega$ ). Considering there are numerous pores and voids in both Si and SE after delithiation as shown in Figures 3 and 4 and Figures S8 and S11 (Supporting Information), the dramatically increased  $R_3$  can be attributed to the structural instability during the delithiation process. The low impedance in Si–SE–C is the result of the stable structure. It is evident that structural stability is essential for Si anode, and the incorporation of SE and carbon can improve its stability, especially under lithiation processes.

Figure 5g compares the cycling performance of three anodes at the current density of  $0.5 \text{ mA cm}^{-2}$ , while the initial three cycles are measured at  $0.2 \text{ mA cm}^{-2}$ . Overall, all three anodes show a gradual decay performance which is mainly attributed to the unstable structure. However, Si–SE–C exhibits the highest capacity. The Si–SE–C delivers the highest discharge/charge capacities of  $2775/2398 \text{ mAh g}^{-1}$  at  $0.2 \text{ mA cm}^{-2}$ . When cycled at  $0.5 \text{ mA cm}^{-2}$ , high discharge/charge capacities of  $2037/1985 \text{ mAh g}^{-1}$  are achieved. After 50 cycles, the capacity gradually decays to  $1137/1136 \text{ mAh g}^{-1}$ . At the same time, discharge/charge capacities of Si–SE reach  $1546/1468 \text{ mAh g}^{-1}$  initially and drop to  $974/940 \text{ mAh g}^{-1}$ . In comparison, the Si shows the lowest discharge/charge capacities of  $1003/946 \text{ mAh g}^{-1}$  which decreases to  $594/593 \text{ mAh g}^{-1}$  after cycling. The higher capacities in Si–SE–C are attributed to the enhanced reaction kinetics in comparison to Si and Si–SE.

The electrochemical performances of the three anodes in full cells are also investigated. The mass loading of NMC is  $14.88 \text{ mg cm}^{-2}$  with an N/P ratio of  $\approx 1.34$ . Figure 5h displays the rate performance of the three cells, where the 1 C equals  $200 \text{ mA g}^{-1}$  based on the mass of NMC. When cycled at C/20, C/10, C/5, C/2, and 1C, the Si–SE–C cell delivers the highest average discharge capacities of 134, 117, 98, 68, and  $45 \text{ mAh g}^{-1}$ . In comparison, the Si–SE cell contributes lower average

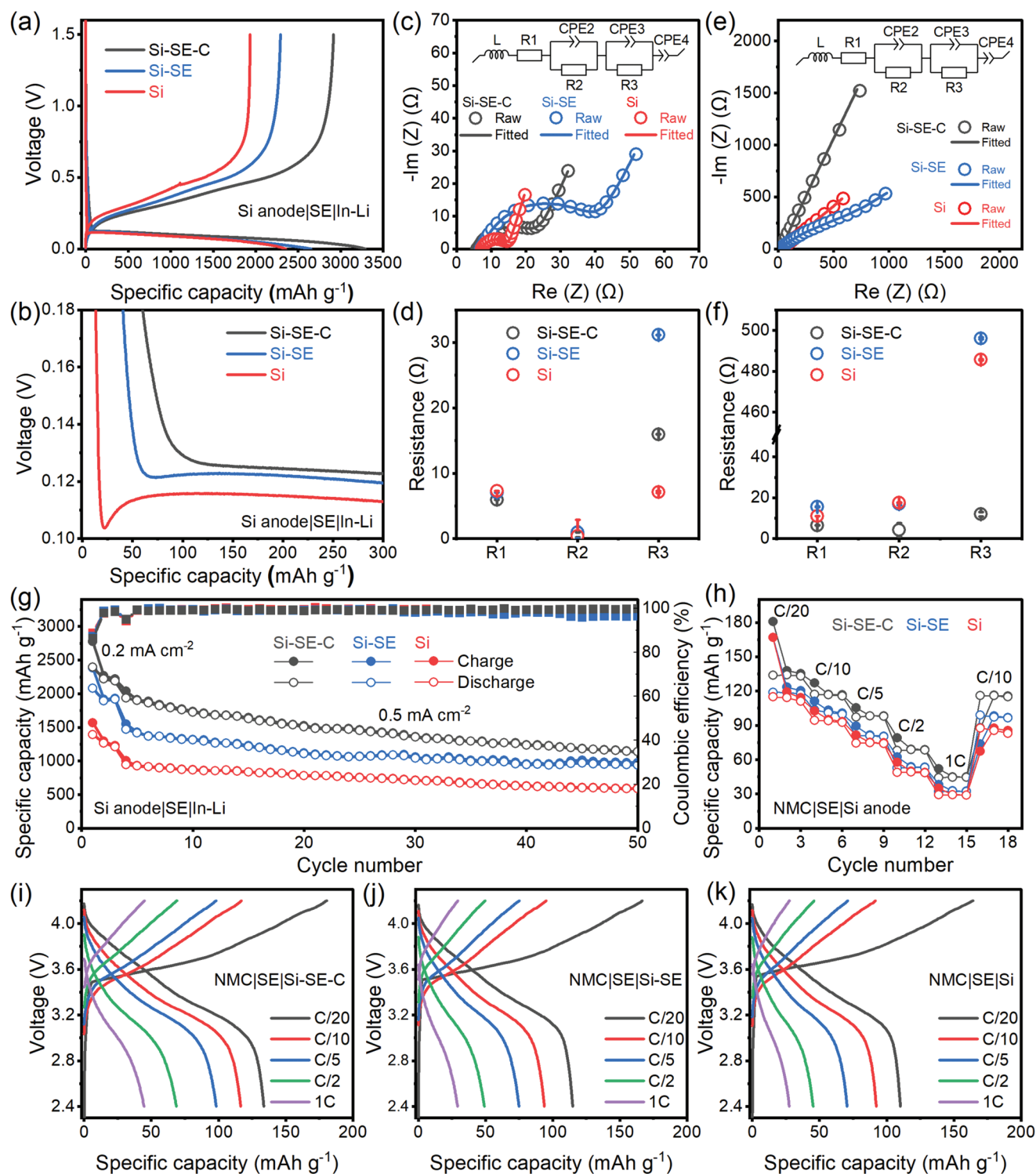


**Figure 5.** Electrochemical performance comparison. a) Galvanostatic charge and discharge profiles of Si-SE-C, Si-SE, and Si anodes in half cells in the initial cycle at the current density of  $0.1 \text{ mA cm}^{-2}$ . b) Zoom-in charge and discharge profiles in (a) to show the overpotential. c) Nyquist plots of three anodes after lithiation and the fitted plots. The inset is the equivalent circuit for fitting. d) Summary of the fitted results in (c). e) Nyquist plots of three anodes after delithiation and the fitted plots. The inset is the equivalent circuit for fitting. f) Summary of the fitted results in (e). f) Cycling performance comparison at the current density of  $0.5 \text{ mA cm}^{-2}$ . g) Rate performance comparison in the full cell. Galvanostatic charge and discharge profiles of the full cells using h) Si-SE-C, i) Si-SE, and j) Si anodes in the rate tests.



capacities of 118, 101, 81, 53, and 32 mAh g<sup>-1</sup>, and the Si cell shows the lowest average capacities of 113, 94, 74, 49, and 29 mAh g<sup>-1</sup> when cycled at same rates. This demonstrates that the addition of SE and carbon can boost the electrochemical performance of the Si anode, which benefits from the enhanced reaction kinetics and improved structural stability aforementioned. Figure 5i–k display the charge and discharge profiles of the three cells at different rates. Interestingly, the Si–SE–C cell delivers the highest initial coulombic efficiency of 74.0%, while the values in Si–SE and Si cells are 71.2% and 68.9%, respectively. Meanwhile, the Si–SE–C cell even shows the best stability in first three cycles (Figure S19, Supporting Information). These results indicate that the decomposition of SE has a negligible effect on the Si anode, with structure stability being a more significant factor.

To better understand the mechanical integrity of three different types of anode materials during lithiation and delithiation processes, a chemo-elasto-plastic model is developed.<sup>[19]</sup> The mathematical model is implemented into an open-source, parallel finite-element tool multiphysics object oriented simulation environment (MOOSE).<sup>[20]</sup> As Si experiences ≈300% volume expansion measured in lattice parameters,<sup>[21]</sup> a large deformation theory is utilized to investigate the chemomechanical behavior of various anode materials. For the kinematics, the deformation gradient can be multiplicatively decomposed as  $F = F_e F_p F_\theta$  in which  $F_e$  denotes the elastic deformation,  $F_p$  is the plastic deformation, and  $F_\theta$  denotes the lithiation/delithiation induced deformation. The permanent plastic deformation of anode materials is captured using a rate independent J2 plasticity model with linear strain hardening behavior. It is assumed that the lithium concentration evolution is governed by Fick's law (where the flux is driven by lithium concentration gradients). For different chemical, elastic, and plastic material properties used in the simulation, one can refer for more details.<sup>[22]</sup> We employed the rule of the mixture to estimate the chemical and mechanical properties of composite anodes (i.e., Si–SE and Si–SE–C) for simplicity.<sup>[23]</sup> As schematic illustration of the boundary conditions to perform the simulations is provided in Figure S20 of the Supporting Information.

Figures 6 and 7 compare the chemomechanical behavior and evolution of volume expansion/contraction along with average effective plastic strain, respectively, for Si, Si–SE, and Si–SE–C anode materials at the end of the lithiation and delithiation stages. Figure 6a,e,i show the pristine reconstructed microstructure for Si, Si–SE, and Si–SE–C anode materials. Figure 6b,f,j clearly depicts the complete insertion and extraction of lithium species from the host lattice. Figure 6c,d illustrates the large effective plastic strain and higher von Mises stresses for the silicon anode due to mechanically constrained colossal volume expansion and contraction (as shown in Figure 7) during the electrochemical cycle. However, the Si–SE anode composite experiences lesser plastic deformation and von Mises stress evolution (Figure 6g,h). SE is much more pliable than Si, thus acting as a mechanical cushion which helps to reduce the stress generated in the Si component. Moreover, the Si–SE–C demonstrates significantly lower plastic deformation and von Mises stress generation because of the meager constrained volume expansion and contraction

(Figure 6k,l). It is because SE and C are much less stiff contrasted to Si and act as stress relaxation mediums within the Si–SE–C composite anode. Other than that, the elastic expansion/contraction of SE and C prior to the beginning of plastic deformation is much more significant than Si. Figure 7 also displays that due to the higher plastic deformation, the Si has not returned to the original  $\Delta V/V_0 = 0$  ratio at the end of delithiation process. However, Si–SE–C has attained the original volume ratio of  $\Delta V/V_0 = 0$  because of the least amount of plastic deformation. Such a mechanism may explain the considerable porosity change reported by experimental analysis for the Si anode (from porosity of ≈27% for pristine to ≈6% at the lithiation stage and ≈15% at delithiation stage) in comparison to the Si–SE and Si–SE–C anode composites. Additionally, the higher von Mises stress generation observed within different anode materials at the end of delithiation stage in contrast to lithiation stage is due to the development of large plastic deformation. It can also arise from the fact that during the lithiation, the diffusion-induced stress generation and applied stack pressure are in the opposite direction, which might reduce the overall elasto-plastic expansion. Nevertheless, the direction of diffusion-induced stress generation and applied stack pressure are the same for the delithiation cycle, which can be responsible for higher plastic deformation and hence the von Mises stress generation. Finally, the results obtained from the above simulations explain that adding SE and C into Si can be a viable alternative for better mechanical stability of Si-based anode materials.

### 3. Conclusion

In conclusion, the electrochemical and mechanical evolutions of nano-Si composite anodes in sulfide SE-based ASLBs are systematically investigated through operando synchrotron XANES, ex situ SEM, and ex situ synchrotron XnT. The operando XANES revealed that the sulfide SE experiences an electrochemical decomposition in the Si anode, and the addition of carbon accelerates this process. This negligible electrochemical decomposition only occurs at the first lithiation process and the products are stable in the following cycles. The ex situ SEM and ex situ XnT evidence that the addition of SE and carbon in the Si anode benefits the mechanical structural stability. A chemo-elasto-plastic model reveals that the addition of softer SE and carbon can relieve the diffusion-induced stresses contributing to better mechanical stability.

Owing to the enhanced reaction kinetics and mechanical structural stability, the Si–SE–C achieved the highest Si utilization, with a lithiation/delithiation capacity of 3288/2917 mAh g<sup>-1</sup> and an initial coulombic efficiency of 88.7%, which are significantly higher than the capacities of 2653/2291 mAh g<sup>-1</sup> and ICE of 86.4% in Si–SE, and the capacities of 2353/1935 mAh g<sup>-1</sup> and ICE of 82.2% in Si. This work indicated that the addition of SE and carbon into nano-Si anode can enhance the reaction kinetics, improve the utilization of Si, and benefit the mechanical structure stability. Although the SE shows slight decomposition, the generated chemistry is ionically conductive and stable in the following cycles. This study is

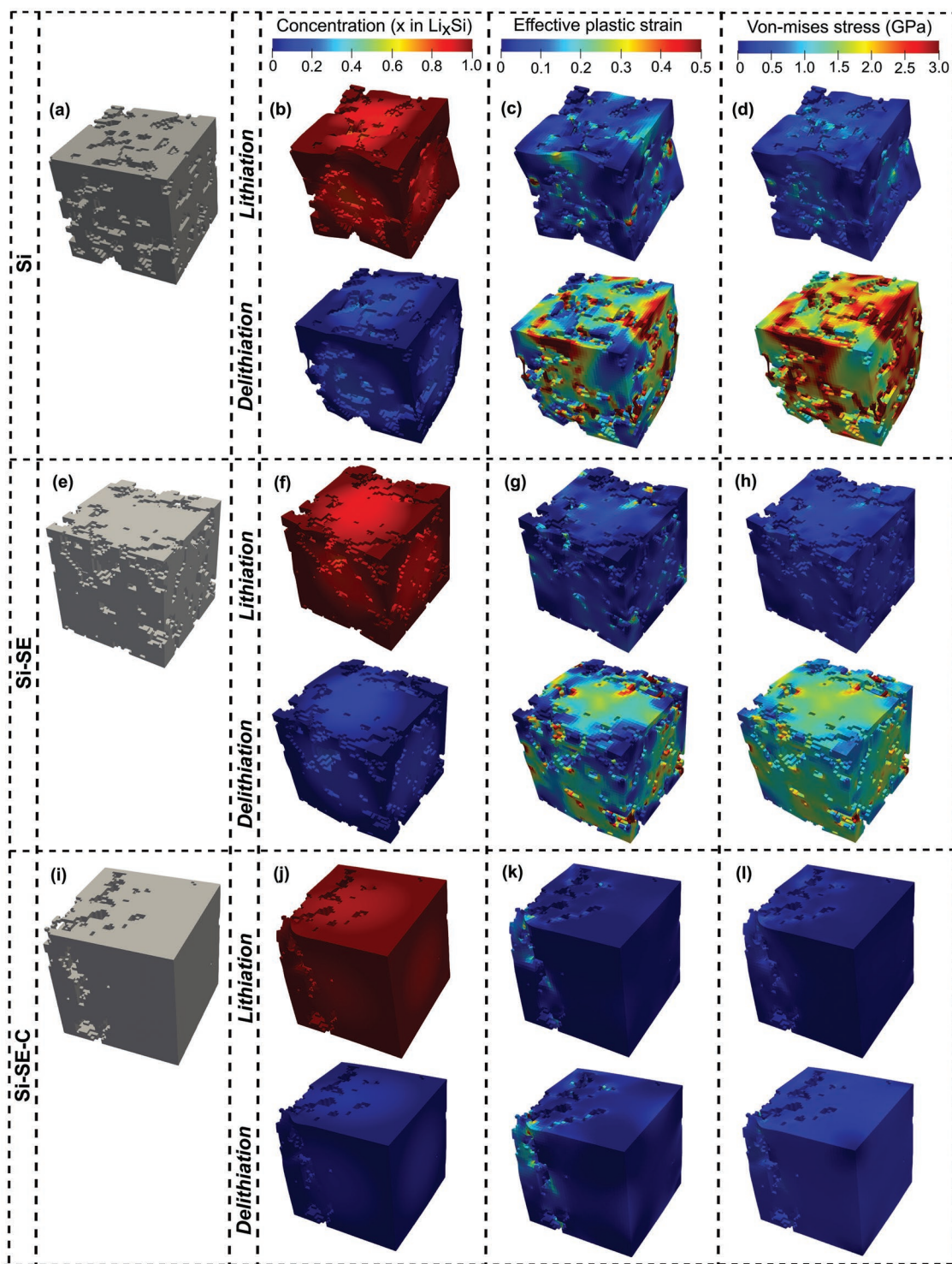


**Figure 6.** Structure evolution investigation using a chemo-elasto-plastic modeling framework for large deformation. Reconstructed 3D microstructure of pristine a) Si, e) Si-SE, and i) Si-SE-C anode materials. For three types of anode materials b,f,j) lithium concentration, c,g,k) effective plastic strain, and d,h,l) von Mises stresses at the end of lithiation and delithiation stages.

concentrated on nano-Si, and it should be taken into consideration that the charge transfer, reaction kinetics, and stability of micro-Si will be distinct from nano-Si, thus necessitating individual studies.

#### 4. Experimental Section

**Material Preparation:** The argyrodite  $\text{Li}_{5.4}\text{PS}_{4.4}\text{Cl}_{1.6}$  was synthesized based on the previous work.<sup>[24]</sup> Briefly,  $\text{Li}_2\text{S}$  (Sigma-Aldrich, 99.98%),  $\text{P}_2\text{S}_5$  (Sigma-Aldrich, 99%), and  $\text{LiCl}$  (Sigma-Aldrich, 99%) were

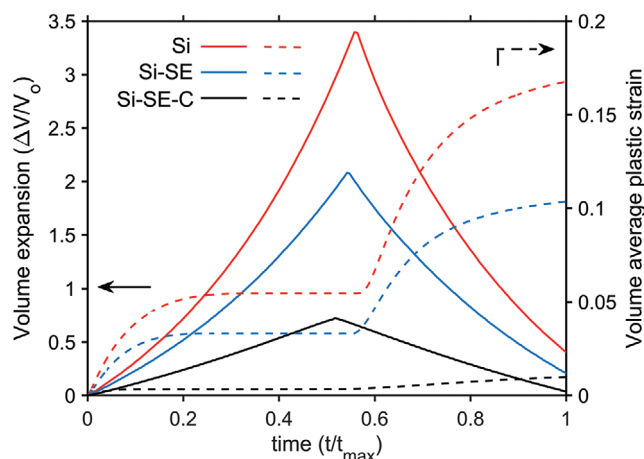


**Figure 7.** Volume expansion and contraction along with the volume average of effective plastic strain for different anode materials during the lithiation.

stoichiometrically mixed through a ball milling for 10 h at 500 rpm. After that, the mixture was annealed at 510 °C for 2 h.

Si composite anodes were prepared by ball milling method. For the Si-SE-C, the 180 mg Si powder (Nanostructured and Amorphous Materials, Inc.), 90 mg of  $\text{Li}_{5.4}\text{PS}_{4.4}\text{Cl}_{1.6}$ , and 30 mg of carbon black (acetylene, 99.9%, Fisher Scientific) were mixed through ball milling for 5 h at 400 rpm under argon atmosphere. For the Si-SE, 210 mg of Si powder and 90 mg of  $\text{Li}_{5.4}\text{PS}_{4.4}\text{Cl}_{1.6}$  were mixed through the same method.

The  $\text{Li}_2\text{SiO}_x$ -coated single-crystal NMC was prepared by the wet-chemical method as in the previous work.<sup>[11]</sup> Tetraethyl orthosilicate (Sigma-Aldrich,  $\geq 99.0\%$ ), lithium (Li, Sigma-Aldrich, 99.9%), anhydrous ethanol (Sigma-Aldrich), and single-crystal NMC 811 (Nanoramic Inc.) were utilized. The NMC cathode material was prepared by mixing 150 mg of  $\text{Li}_2\text{SiO}_x$ -coated single-crystal NMC with 50 mg  $\text{Li}_{5.4}\text{PS}_{4.4}\text{Cl}_{1.6}$  by grinding for 10 min.

**Battery Assembling and Electrochemical Characterization:** ASLBs were fabricated by a cold pressing method inside the glovebox. To fabricate the Si half cells, 150 mg of  $\text{Li}_{5.4}\text{PS}_{4.4}\text{Cl}_{1.6}$  was pressed in PEEK die with a diameter of 12.7 mm under the pressure of 300 MPa. Then different amounts of the anode material (3.0 mg of Si-SE-C, 2.6 mg of Si-SE, or 1.8 mg of Si) were cast on one side of the  $\text{Li}_{5.4}\text{PS}_{4.4}\text{Cl}_{1.6}$ . A piece of In-Li was placed on the other side. The copper foil was used as the current collector for both sides. The cell was further pelletized at 150 MPa by two stainless steel plugs in a stainless-steel framework. The specific capacity was calculated based on the weight of Si. The NMC-Si full cells were assembled through the same method with Si half cells. Instead of In-Li, 25 mg of NMC cathode material was cast on the other side of SE with a piece of aluminum foil as the current collector. All cells were rested for 5 h before electrochemical tests. The galvanostatic charge and discharge tests were conducted at room temperature between 0 to 1.5 V (vs  $\text{Li}/\text{Li}^+$ ) for the Si half cell and between 2.4 and 4.2 V (vs  $\text{Li}/\text{Li}^+$ ) for the full cell. EIS was conducted on a Biologic SP150 potentiostat (Biologic, France). The measurement was carried out at frequencies from 1 MHz to 10 mHz with an AC amplitude of 10 mV. CV was carried out on MPG2 potentiostat (Biologic, France) in the range of 0–1.5 V (vs  $\text{Li}^+/\text{Li}$ ) at a scan rate of 0.1  $\text{mV s}^{-1}$ .

The operando XANES was conducted in full cells based on Si-SE and Si-SE-C anodes separately. In detail, 60 mg of  $\text{Li}_{5.4}\text{PS}_{4.4}\text{Cl}_{1.6}$  was pressed into a pellet in a homemade cell under the pressure of 300 MPa. Then NMC cathode and anode powder were cast onto both sides severally. Then 150 MPa of pressure was applied by a framework. The mass loading of NMC and Si are 46.8 and 3.75  $\text{mg cm}^{-2}$ , separately. The cells are galvanostatic charged and discharged in the voltage range from 2.4 to 4.2 V at the current rate of  $C/10$ . Here 1 C equals 200  $\text{mA g}^{-1}$ . The

specific capacity was calculated based on the weight of NMC. The state (0%, 25%, 50%, 75%, 100%) was defined according to the SoC and DoD in the battery test.

**Material Characterizations:** The SEM images were conducted on a scanning electron microscope (S4800, Hitachi). The accelerating voltage was 3 kV with a work distance of 8 mm. The energy-dispersive X-ray spectroscopy mapping was carried out on the same equipment with an accelerating voltage of 15 kV and a working distance of 15 mm. XRD was measured on PANalytical/Philips X'Pert Pro (PANalytical, The Netherlands) with  $\text{Cu K}\alpha$  radiation.

XANES spectroscopy was conducted on the tender energy X-ray absorption spectroscopy (TES, 8-BM) beamline of the National Synchrotron Light Source II (NSLS-II) at Brookhaven National Laboratory. For the operando XANES spectra collection, a custom-designed cell with a side window was fabricated as mentioned above. The Athena software package was utilized to process the data.<sup>[24]</sup>

The ex situ XnT was conducted on the full field X-ray imaging (FXI, 18-ID) beamline of National Synchrotron Light Source II at Brookhaven National Laboratory. The XnT sample was sealed in the Kapton tube with a diameter of 1 mm in the argon atmosphere. A scientific package, TXM-Sandbox, was used to reconstruct and align the tomographic datasets.<sup>[26]</sup> ORS Dragonfly software was used to reconstruct the 3D images.

**Microstructure Reconstruction:** Microstructure samples cut from the segmented XnT images are converted to finite-element meshes (Figure S21, Supporting Information). Each voxel is converted to an 8-node solid element. A structure connectivity analysis is conducted to identify and eliminate the disconnected solid elements that are “floating” in the 3D space. The volume fraction of the microstructure model is verified by dividing the number of solid elements by the total number of voxels of the corresponding image cube.

**Governing Equations:** A brief description of kinematics, constitutive relations, and governing equations is outlined here. For more detailed version, one can refer the work of Pal et al.<sup>[27]</sup> To account for the large deformation of silicon anode during the lithiation/delithiation reaction, the multiplicative decomposition of the total deformation gradient is defined as

$$\mathbf{F} = \mathbf{F}_e \mathbf{F}_\theta \mathbf{F}_p \quad (1)$$

in which  $\mathbf{F}_e$ ,  $\mathbf{F}_\theta$ , and  $\mathbf{F}_p$  are deformation gradients associated with the shape change due to the reversible elastic deformation, an insertion and extraction of lithium species, and an irreversible plastic deformation of underlying material, respectively. It is assumed that the lithiation-induced deformation is dilatational and expressed as

$$\mathbf{F}_\theta = (1 + \beta c)^{1/3} \mathbf{I} \quad (2)$$

where  $\beta$  denotes the expansion coefficient, and  $\mathbf{I}$  is the identity matrix. The spatial velocity gradient can be additively decomposed into three contributions as

$$\mathbf{L} = \mathbf{L}_e + \mathbf{L}_\theta + \mathbf{L}_p \quad (3)$$

with  $\mathbf{L}_e = \dot{\mathbf{F}}_e \mathbf{F}_e^{-1}$ ,  $\mathbf{L}_\theta = \mathbf{F}_e \mathbf{F}_\theta \dot{\mathbf{F}}_\theta^{-1} \mathbf{F}_e^{-1}$ , and  $\mathbf{L}_p = \mathbf{F}_e \mathbf{F}_\theta \dot{\mathbf{F}}_p \mathbf{F}_p^{-1} \mathbf{F}_\theta^{-1} \mathbf{F}_e^{-1}$ . The mass conservation of lithium is considered for solving the concentration of lithium species within electrode material as

$$\partial_t c + \nabla \cdot \mathbf{J} = 0 \text{ in } \Omega \quad (4)$$

in which  $\mathbf{J}$  defines the diffusive flux of lithium. Initial and boundary conditions for the diffusion of lithium within the host lattice are described as follows

$$c(t=0) = c_0 \text{ on } \partial\Omega_c, \text{ and } \mathbf{J} \cdot \mathbf{n} = J_p \text{ on } \partial\Omega_J \quad (5)$$

with  $c_0$  denotes the initial concentration, and  $J_p$  is the applied flux to the surface with normal  $\mathbf{n}$ . For isotropic diffusion, the intercalating lithium flux in the electrode material is defined as

$$\mathbf{J} = -D\nabla c \quad (6)$$

in which  $D$  denotes the diffusivity of lithium species within the electrode material. Moreover, to determine the deformed shape and stress generation during the lithiation and delithiation process, the balance of linear momentum (or mechanical equilibrium) is expressed as

$$\nabla \cdot \mathbf{P} = 0 \text{ in } \Omega \text{ with } \mathbf{P} = \mathbf{F}\mathbf{S} \quad (7)$$

where  $\mathbf{P}$  and  $\mathbf{S}$  are the first and second Piola–Kirchhoff stress tensors. The boundary conditions for mechanical equilibrium are represented as  $\mathbf{P}\mathbf{n} = \mathbf{t}$  on  $\partial\Omega_t$  and  $\mathbf{u} = \mathbf{u}_p$  on  $\partial\Omega_u$ . In conjunction with intercalation/deintercalation of lithium, an inelastic response of the electrode is assumed to obey the J2-flow rule. Accordingly, the plastic deformation gradient  $\mathbf{L}_p$  is described as

$$\mathbf{L}_p = \dot{\mathbf{F}}_p \mathbf{F}_p^{-1} = \dot{\lambda} \mathbf{N}_p \text{ with } \mathbf{N}_p = \frac{\partial f}{\partial \mathbf{M}} \quad (8)$$

in which,  $\mathbf{N}_p$  represents the direction of plastic flow,  $\dot{\lambda}$  is the equivalent plastic rate, and  $\mathbf{M}$  is the Mandel stress. In the above equation, the yield function  $f$  for linearly isotropic hardening case is considered and is expressed as

$$f(\boldsymbol{\sigma}, \bar{\boldsymbol{\epsilon}}_p) = \sqrt{\frac{3}{2} \mathbf{M}_d : \mathbf{M}_d} - (\sigma_y + H\bar{\boldsymbol{\epsilon}}_p) \quad (9)$$

with  $\mathbf{M}_d$  is the deviatoric part of the Mandel stress,  $\sigma_y$  is the yield strength, and  $H$  is the hardening modulus for the material.

**Simulation Parameters:** This section provides the mechanical and transport properties utilized to perform the simulations. The elastic modulus of the silicon was chosen to be concentration dependent with the value of  $E_{\text{lithiated}} = 12$  GPa at the fully lithiated state and  $E_{\text{delithiated}} = 160$  GPa at completely delithiated state. Poisson's ratio of lithiated and delithiated Si was taken as 0.28. The elastic modulus for SE and C was assumed to be 10 GPa and 12.8 MPa, respectively. Nonetheless, Poisson's ratio for SE and C was considered 0.28. Both Si and SE were taken to be elasto-plastic type; however, C was assumed to exhibit only elastic deformation. Accordingly, the yield strength and hardening modulus of Si was chosen to be 1 and 5 GPa. Moreover, the SE was considered a perfectly plastic material with the yield strength of 200 MPa. The expansion coefficient  $\beta$  for Si was calculated based on the 400% volume expansion. Nevertheless, the volume expansion of SE and C materials was not considered. The diffusivity coefficient and maximum stoichiometric concentration of the Si were assumed to be  $10^{-16} \text{ m}^2 \text{ s}^{-1}$  and  $365100 \text{ mol m}^{-3}$ , respectively. Chemical and mechanical properties for both Si–SE and Si–SE–C composites were obtained using the volume fraction of individual components within anode materials. However, the SE and C were considered to be inactive for the diffusion phenomena for the sake of simplicity.

## Supporting Information

Supporting Information is available from the Wiley Online Library or from the author.

## Acknowledgements

D.C., T.J., and A.S. contributed equally to this work. H.Z. acknowledges the financial support from National Science Foundation under Award No. CBET-ES-1924534. A.S. and J.Z. are grateful to the financial support of NASA 19-TTT-0103 project (Award No. 80NSSC21M0114). This research used 8-BM of the National Synchrotron Light Source II, a U.S. Department of Energy (DOE) Office of Science User Facility operated for the DOE Office of Science by Brookhaven National Laboratory under Contract No. DE-SC0012704. This research used resources 18-ID (FXI) of the National Synchrotron Light Source II, a U.S. Department

of Energy (DOE) Office of Science User Facility operated for the DOE Office of Science by Brookhaven National Laboratory under Contract No. DE-SC0012704. The authors acknowledge the Boston Electron Microscopy Center at Northeastern University for the use of SEM facility. The authors would like to acknowledge the Northeastern University Center for Renewable Energy Technology for the use of XRD facility.

## Conflict of Interest

The authors declare no conflict of interest.

## Data Availability Statement

Research data are not shared.

## Keywords

all-solid-state batteries, nano-Si anodes, operando investigation, sulfide solid-state electrolytes, XANES, X-ray nanotomography

Received: November 21, 2022

Revised: January 10, 2023

Published online:

- [1] A. Kwade, W. Haselrieder, R. Leithoff, A. Modlinger, F. Dietrich, K. Droeder, *Nat. Energy* **2018**, *3*, 290.
- [2] a) J. W. Choi, D. Aurbach, *Nat. Rev. Mater.* **2016**, *1*, 16013; b) C. P. Grey, D. S. Hall, *Nat. Commun.* **2020**, *11*, 6279.
- [3] a) D. Cao, X. Sun, Y. Wang, H. Zhu, *Energy Storage Mater.* **2022**, *48*, 458; b) D. Cao, Y. Zhao, X. Sun, A. Natan, Y. Wang, P. Xiang, W. Wang, H. Zhu, *ACS Energy Lett.* **2020**, *5*, 3468.
- [4] L. Wang, Z. Wu, J. Zou, P. Gao, X. Niu, H. Li, L. Chen, *Joule* **2019**, *3*, 2086.
- [5] M. Ashuri, Q. He, L. L. Shaw, *Nanoscale* **2016**, *8*, 74.
- [6] a) P. H. L. Notten, F. Roozeboom, R. A. H. Niessen, L. Baggetto, *Adv. Mater.* **2007**, *19*, 4564; b) R. B. Cervera, N. Suzuki, T. Ohnishi, M. Osada, K. Mitsuishi, T. Kambara, K. Takada, *Energy Environ. Sci.* **2014**, *7*, 662; c) R. Miyazaki, N. Ohta, T. Ohnishi, I. Sakaguchi, K. Takada, *J. Power Sources* **2014**, *272*, 541.
- [7] N. Ohta, S. Kimura, J. Sakabe, K. Mitsuishi, T. Ohnishi, K. Takada, *ACS Appl. Energy Mater.* **2019**, *2*, 7005.
- [8] a) D. H. Kim, H. A. Lee, Y. B. Song, J. W. Park, S.-M. Lee, Y. S. Jung, *J. Power Sources* **2019**, *426*, 143; b) D. H. S. Tan, Y.-T. Chen, H. Yang, W. Bao, B. Sreenarayanan, J.-M. Doux, W. Li, B. Lu, S.-Y. Ham, B. Sayahpour, J. Scharf, E. A. Wu, G. Deysler, H. E. Han, H. J. Hah, H. Jeong, J. B. Lee, Z. Chen, Y. S. Meng, *Science* **2021**, *373*, 1494.
- [9] H. Huo, J. Janek, *ACS Energy Lett.* **2022**, *7*, 4005.
- [10] Q. Zhang, D. Cao, Y. Ma, A. Natan, P. Aurora, H. Zhu, *Adv. Mater.* **2019**, *31*, 1901131.
- [11] D. Cao, X. Sun, Y. Li, A. Anderson, W. Lu, H. Zhu, *Adv. Mater.* **2022**, *34*, 2200401.
- [12] a) N. A. Dunlap, S. Kim, J. J. Jeong, K. H. Oh, S.-H. Lee, *Solid State Ion.* **2018**, *324*, 207; b) H. Liu, Q. Sun, H. Zhang, J. Cheng, Y. Li, Z. Zeng, S. Zhang, X. Xu, F. Ji, D. Li, *Energy Storage Mater.* **2022**, *55*, 244.
- [13] L. Sun, Y. Liu, R. Shao, J. Wu, R. Jiang, Z. Jin, *Energy Storage Mater.* **2022**, *46*, 482.
- [14] E. Sivonxay, M. Aykol, K. A. Persson, *Electrochim. Acta* **2020**, *331*, 135344.

- [15] D. H. Tan, E. A. Wu, H. Nguyen, Z. Chen, M. A. Marple, J.-M. Doux, X. Wang, H. Yang, A. Banerjee, Y. S. Meng, *ACS Energy Lett.* **2019**, *4*, 2418.
- [16] T. K. Schwietert, V. A. Arszewska, C. Wang, C. Yu, A. Vasileiadis, N. J. J. de Klerk, J. Hageman, T. Hupfer, I. Kerkamm, Y. Xu, E. van der Maas, E. M. Kelder, S. Ganapathy, M. Wagemaker, *Nat. Mater.* **2020**, *19*, 428.
- [17] D. Paganin, S. C. Mayo, T. E. Gureyev, P. R. Miller, S. W. Wilkins, *J. Microsc.* **2002**, *206*, 33.
- [18] S. Spence, W.-K. Lee, F. Lin, X. Xiao, *Nanotechnology* **2021**, *32*, 442003.
- [19] H. Yang, F. Fan, W. Liang, X. Guo, T. Zhu, S. Zhang, *J. Mech. Phys. Solids* **2014**, *70*, 349.
- [20] a) D. Gaston, C. Newman, G. Hansen, D. Lebrun-Grandie, *Nucl. Eng. Des.* **2009**, *239*, 1768; b) C. J. Permann, D. R. Gaston, D. Andrš, R. W. Carlsen, F. Kong, A. D. Lindsay, J. M. Miller, J. W. Peterson, A. E. Slaughter, R. H. Stogner, *SoftwareX* **2020**, *11*, 100430.
- [21] L. Beaulieu, K. Eberman, R. Turner, L. Krause, J. Dahn, *Electrochem. Solid-State Lett.* **2001**, *4*, A137.
- [22] a) M. Pharr, K. Zhao, X. Wang, Z. Suo, J. J. Vlassak, *Nano Lett.* **2012**, *12*, 5039; b) C. E. Athanasiou, X. Liu, M. Y. Jin, E. Nimon, S. Visco, C. Lee, M. Park, J. Yun, N. P. Padture, H. Gao, *Cell Rep. Phys. Sci.* **2022**, *3*, 100845.
- [23] T. W. Clyne, D. Hull, *An Introduction to Composite Materials*, Cambridge University Press, Cambridge **2019**.
- [24] X. Sun, D. Cao, Y. Wang, T. Ji, W. Liang, H. Zhu, *Adv. Mater. Interfaces* **2022**, *9*, 2200539.
- [25] M. Newville, B. Ravel, *J. Synchrotron Radiat.* **2005**, *12*, 537.
- [26] X. Xiao, Z. Xu, F. Lin, W.-K. Lee, *J. Synchrotron Radiat.* **2022**, *29*, 266.
- [27] a) S. Pal, S. S. Damle, P. N. Kumta, S. Maiti, *Comput. Mater. Sci.* **2013**, *79*, 877; b) A. F. Bower, P. Guduru, *Modell. Simul. Mater. Sci. Eng.* **2012**, *20*, 045004.